Chemical Science

ROYAL SOCIETY OF CHEMISTRY

EDGE ARTICLE

View Article Online
View Journal | View Issue

Cite this: *Chem. Sci.*, 2025, **16**, 10487

All publication charges for this article have been paid for by the Royal Society of Chemistry

Received 20th September 2024
Accepted 24th April 2025

DOI: 10.1039/d4sc06373b

rsc.li/chemical-science

An amine electrolyte additive with claw structure promoting the stability of a Zn anode in aqueous batteries†

Xiaoqi Sun, *[ab] Hongtu Zhan,[a] Qianrui Li[a] and Kuo Wang*[a]

The Zn metal anode in aqueous Zn batteries suffers a number of challenges, including dendritic deposition and parasitic reactions. Here, we present a facile interface regulation strategy using a low concentration of electrolyte additive of 0.5 wt% tris(3-aminopropyl)amine (TAA). The TAA molecule exhibits a claw structure with an electronegative amino site at each end. It allows a strong anchorage on the surface of Zn and regulation of Zn^{2+} solvation structures near the interface. This allows easier removal of solvated water, but makes final TAA removal more difficult, thereby suppressing side reactions and controlling deposition kinetics. Furthermore, the TAA molecule exhibits strong affinity on the (100) plane of Zn which is twice of the one on (002). It promotes a preferred growth orientation and generates uniform deposits. Benefitting from the above positive effects of the TAA additive, the cycle life of a Zn symmetric cell extends to 8.6 times that in the baseline electrolyte. The cycle life of a full battery using a commercial V_2O_5 cathode is also effectively increased.

Introduction

Aqueous Zn batteries are considered promising competitors for grid-scale energy storage thanks to their high safety and low cost.[1–12] The Zn metal anode delivers low redox potential (−0.76 V *vs.* standard hydrogen electrode) and high theoretical capacity (820 mA h g^{-1}/5855 mA h cm^{-3}). Unfortunately, it suffers inevitable parasitic reactions in aqueous electrolytes and rampant dendritic growth.[13–18] They seriously damage the stability of the Zn electrode and hinder the applications of Zn batteries. To solve the above issues, researchers have recently carried out a series of modification strategies, mainly including artificial interface layer protection and electrolyte modification. The former enables a more stable electrode/electrolyte interface by blocking their physical contact and homogenizes Zn^{2+} transport within the interface layer. Nevertheless, the adhesion properties and tolerance to volume change need to be carefully controlled. Conversely, the electrolyte modification strategy provides a self-adapted dynamic protection effect. For instance, electrolyte additives/co-solvents of NTE,[19] TU,[20] Ace,[21] DEC[22] and SL[23] have been shown to regulate the Zn surface environment, enter Zn^{2+} solvation structures, and/or modify the hydrogen bonding network, which endows the Zn electrode with enhanced cycling stability. Notably, the content of additives needs to be controlled at a low level to maintain the bulk aqueous nature and its associated advantages.

As electrochemical reactions take place at the Zn electrode and electrolyte interface, additives that are able to accumulate at the interface and modify the local environment would help to reduce the required amount of additives. Based on this consideration, we herein present an additive of 0.5 wt% tris(3-aminopropyl)amine (TAA) as an interface regulator for the Zn electrode in conventional 2 mol kg^{-1} (m) $ZnSO_4$ electrolyte. In the TAA molecule, the central nitrogen connects with three aminopropyl chains with electronegative nitrogen ends, possessing up to four active sites. It allows strong anchorage on the Zn surface as well as the participation in Zn^{2+} solvation structures at the nearby interface. It not only homogenizes cation flux towards the electrode but also modifies the subsequent desolvation process. As a result, the removal of solvated water is facilitated in TAA-containing structures, which inhibits the hydrogen evolution reaction (HER). Additionally, the final desolvation of TAA requires a higher energy barrier, and the deposition kinetics are modulated. Meanwhile, the TAA molecule exhibits greater affinity on the (100) plane of Zn, which promotes a preferred deposition orientation and generates uniform deposits. Benefitting from these effects of the 0.5 wt% TAA additive, the cycle life of a Zn symmetric cell extends to 8.6 times that of the baseline electrolyte. The cycle life of a full battery using a commercial V_2O_5 cathode is also effectively improved.

[a]*Department of Chemistry, Northeastern University, Shenyang 110819, China. E-mail: sunxiaoqi@mail.neu.edu.cn; 2110043@stu.neu.edu.cn*

[b]*National Frontiers Science Center for Industrial Intelligence and Systems Optimization, Northeastern University, 3-11 Wenhua Road, Shenyang, 110819, China*

† Electronic supplementary information (ESI) available. See DOI: https://doi.org/10.1039/d4sc06373b

Results

Fig. 1a shows the molecular structure and calculated electrostatic potential (ESP) of the TAA molecule. The central nitrogen is connected with three aminopropyl chains. Negative ESP regions are located at the three ends as well as the central nitrogen atoms, indicating their ability to coordinate with Zn and Zn^{2+}. The adsorption behavior of the TAA molecule on Zn foil is first analyzed through experimental characterizations and theoretical calculations. The electrochemical double layer capacitance (EDLC) of the Zn electrode in the baseline 2 m $ZnSO_4$ electrolyte and after the addition of 0.5 wt% TAA is evaluated by cyclic voltammetry (CV) scans in the non-Faraday range (Fig. S1,† electrolytes labeled as no TAA and 0.5-TAA, respectively). According to linear fits, the EDLC is 67 μF cm^{-2} in the 0.5-TAA electrolyte, a value lower than the 128 μF cm^{-2} in the baseline electrolyte (Fig. 1b). This suggests that interface water molecules are replaced by TAA molecules of larger size, extending the distance of the Stern layer.[24,25] To further verify the adsorption ability of TAA molecules on the Zn surface, Zn foil is immersed in deionized water and 0.5 wt% TAA solutions, respectively. The surface becomes corroded after soaking in water, as shown in the scanning electron microscopy (SEM) image, and the side-product of ZnO is recognized by X-ray diffraction (XRD, Fig. 1c and d). This suggests a chemical displacement reaction between protons and Zn that causes an increase in pH and ZnO formation. By contrast, the Zn surface remains flat and no ZnO is detected by XRD with the addition of 0.5 wt% TAA. The additive also suppresses by-product formation in the 2 m $ZnSO_4$ solution (Fig. S2†). In the energy dispersive X-ray spectroscopy (EDS) mapping of Zn soaked in 0.5 wt% TAA solution, uniform distributions of C and N elements are observed (Fig. S3†). The surface environment is further characterized by X-ray photoelectron spectroscopy (XPS, Fig. 1e), which reveals the N–C component in both N 1s and C 1s spectra. These results suggest the adsorption of the TAA molecule on the surface of Zn. The adsorption behaviors of H_2O and TAA on the Zn surface are studied using density functional theory (DFT) calculations. As shown in Fig. 1f, TAA exhibits a much stronger interaction energy of −1.21 eV than the

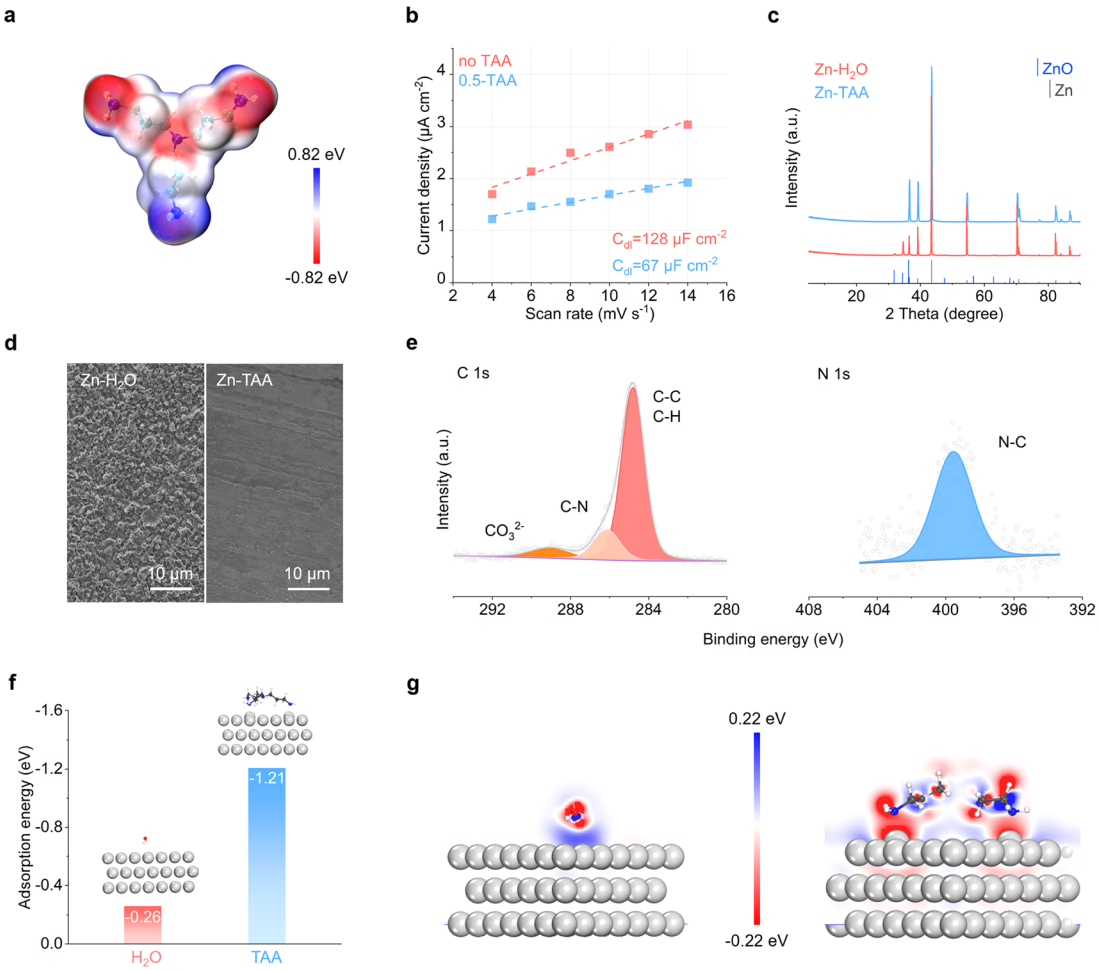

Fig. 1 (a) Molecular structure and ESP map of the TAA molecule. (b) Linear fits to calculate the EDLC of the Zn electrode in 2 m $ZnSO_4$ without or with 0.5 wt% TAA additive. (c) XRD patterns and (d) SEM images of Zn immersed in water or 0.5 wt% TAA solution for 48 hours. (e) The C 1s and N 1s XPS of Zn immersed in 0.5 wt% TAA solution for 48 hours. (f) The adsorption energies of H_2O and TAA molecules on the surface of Zn and (g) the corresponding 2D contour map of electron density statistics.

−0.26 eV for water, suggesting the preferential adsorption of the former. The adsorption abilities are also shown by the 2D contour map of electron density statistics, demonstrating strong electron exchange at the side amino sites of TAA (Fig. 1g). Therefore, the TAA additive functions as an effective anchorage on the Zn surface, which creates a locally additive-rich environment and suppresses corrosion processes.

Considering the strong electron-donating ability of nitrogen sites, the adsorbed TAA molecules would also interact with Zn^{2+} at the nearby interface. Fig. 2a compares the ^{13}C nuclear magnetic resonance (NMR) spectra of 0.5 wt% TAA solutions without and with the addition of $ZnSO_4$ salt. Following the introduction of $ZnSO_4$, up-field shifts are observed for the C peaks of TAA, suggesting the coordination of adjacent nitrogen sites with the added Zn^{2+}. The solvation structures of Zn^{2+} in the 0.5-TAA electrolyte are studied using molecular dynamic (MD) simulation (Fig. 2b). In the resulting radial distribution function (RDF), the Zn^{2+}–N(TAA-side) peak shows up at around 2 Å, the distance of which is close to Zn^{2+}–O(H_2O). Accordingly, a $[Zn(H_2O)_5TAA]^{2+}$ solvation structure is revealed from the simulation box (Fig. 2c), which presents a stronger relative energy of −17.06 eV compared to −15.76 eV for $[Zn(H_2O)_6]^{2+}$. The coordination between Zn^{2+} and TAA also exhibits a higher bond order than Zn^{2+}–H_2O. These results demonstrate the preferential entrance of TAA into the solvation shell of Zn^{2+}. Considering the adsorption and accumulation of TAA on the surface of Zn, the $Zn(H_2O)_6^{2+}$ structure in the bulk electrolyte tends to spontaneously transform to TAA-participating structures at the TAA-rich interface. Therefore, the amino groups on TAA provide uniform sites for incoming Zn^{2+}, which homogenizes cation flux at the interface.

The regulated Zn^{2+} solvation structures at the interface further modify the subsequent desolvation path. Fig. 2d and S4† summarize the energy barriers along the desolvation steps of $[Zn(H_2O)_6]^{2+}$ and $[Zn(H_2O)_5TAA]^{2+}$. In the former, the barriers gradually increase from 1.20 eV to 4.60 eV upon the release of solvated water. In the latter, water is also desolvated first, though with much lower barriers, ranging from 0.75 eV to 0.97 eV. This easier water removal, together with the higher energy levels of the lowest unoccupied molecular orbital (LUMO) at each step in the TAA-containing structure, help to suppress HER (Fig. 2e). It should be noted that the final desolvation of TAA from Zn^{2+} requires three times the energy relative to that for water. This corresponds to more limited reduction kinetics. This inhibits uncontrollable nucleation or facile cation depletion during Zn deposition, which is beneficial for the formation of uniform deposits.

The detailed Zn deposition behavior is investigated through experimental methods. Fig. 3a shows the evolution of chronoamperometry (CA) curves with an increase in deposition voltage from 5 mV to 200 mV (60 s at each voltage) in the $ZnSO_4$ electrolyte without or with 0.5 wt% TAA additive. During the initial periods at low voltages, the differences between the two curves are relatively small (Fig. S5†). Upon a further increase in voltage, the current density responses in the baseline electrolyte exhibit significant changes, especially from 120 mV. In comparison, the evolution of current remains stable upon the introduction of 0.5 wt% TAA. This corresponds to controlled reduction kinetics and stable deposit morphologies under various conditions in the latter.[26,27] Thus, the TAA additive also results in increased charge transfer resistance at the Zn electrode (Fig. S6†). Fig. 3b compares the change in overpotential with current density under galvanostatic processes in the two electrolytes. According to the linear fits, the exchange current density decreases from 2.83 mA cm^{-2} in the baseline electrolyte to 1.76 mA cm^{-2} in 0.5-TAA. This also supports the idea of regulated Zn deposition behavior following the introduction of TAA.[28] Fig. 3c shows the Tafel plots of the Zn electrode. The corrosion current density is effectively reduced from 349 μA cm^{-2} to 21 μA cm^{-2} after the addition of TAA, demonstrating its anti-corrosion capability.[29,30]

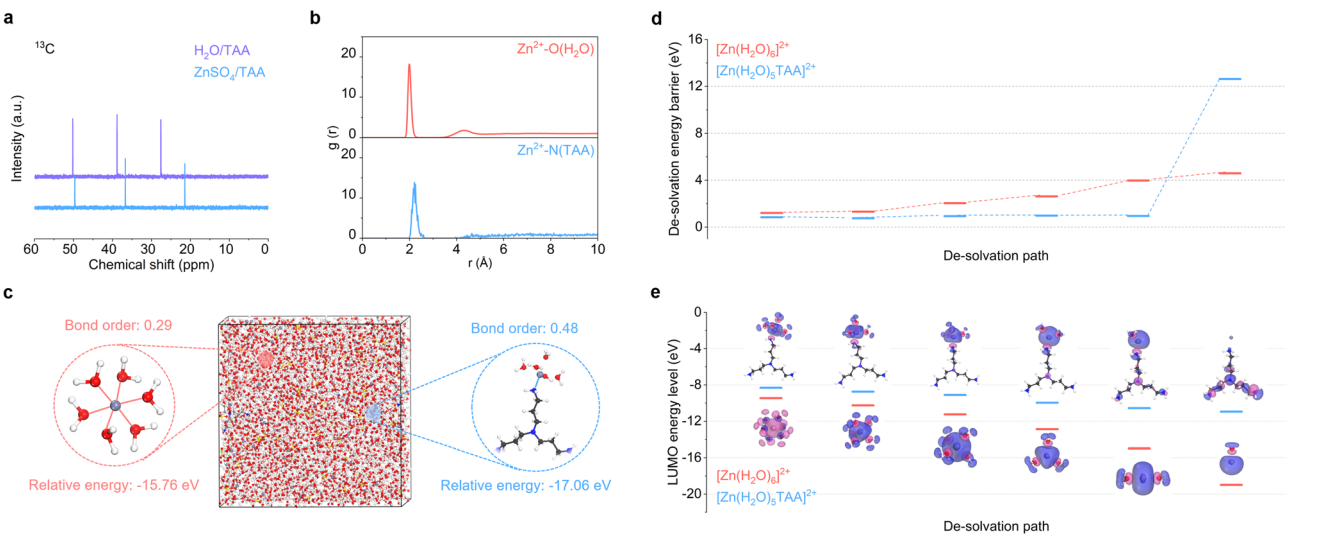

Fig. 2 (a) ^{13}C NMR of 0.5 wt% TAA without and with $ZnSO_4$ salt. (b) RDFs, (c) MD simulation box, together with the structures, relative energies and bond orders of $[Zn(H_2O)_6]^{2+}$ and $[Zn(H_2O)_5TAA]^{2+}$ solvation structures in the $ZnSO_4$ electrolyte with 0.5 wt% TAA additive. (d) Desolvation energy barriers at each step and (e) corresponding LUMO energy levels of $[Zn(H_2O)_6]^{2+}$ and $[Zn(H_2O)_5TAA]^{2+}$.

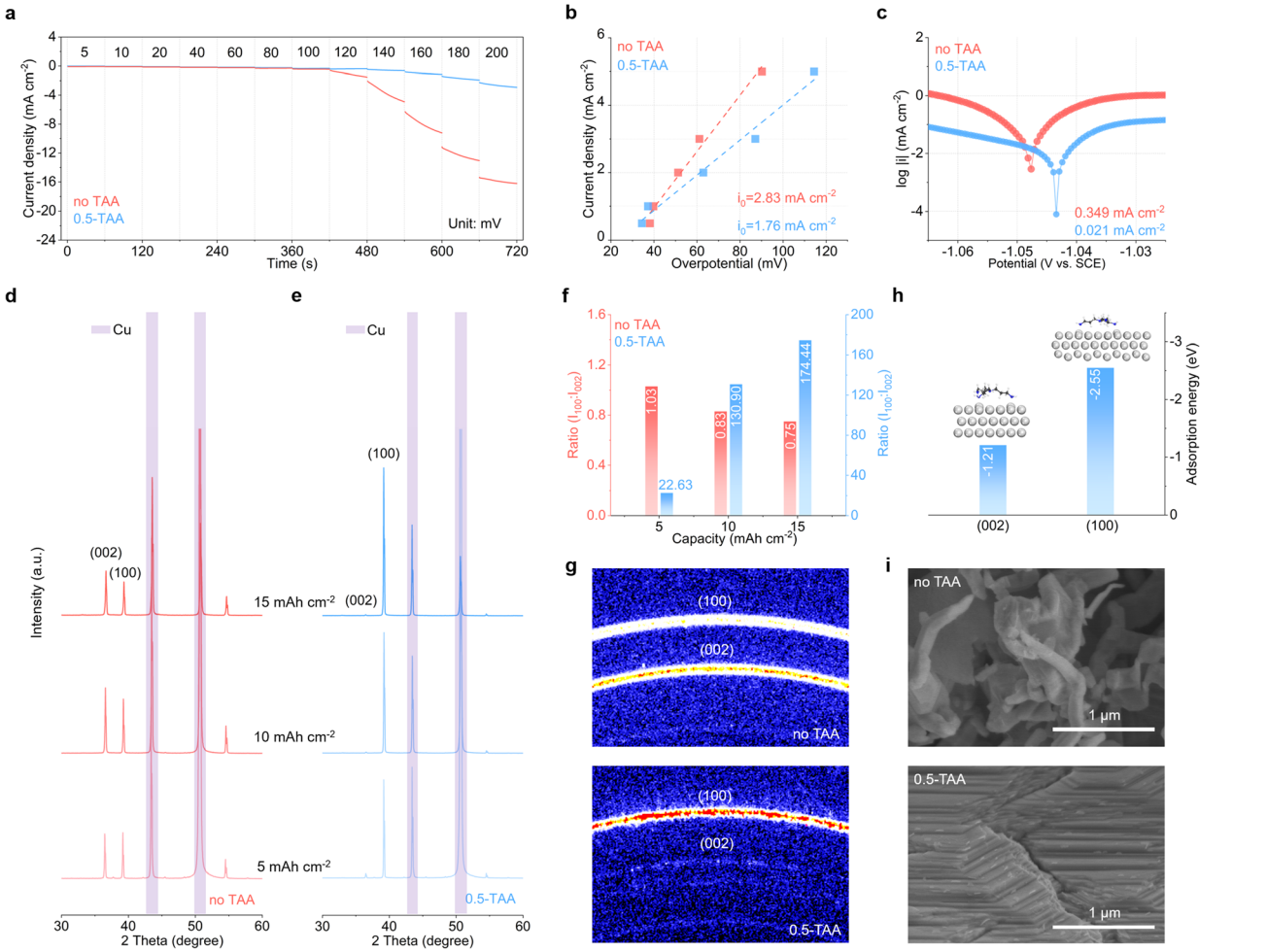

Fig. 3 (a) CA curves at various voltages, (b) exchange current densities, (c) Tafel plots of Zn electrodes in 2 m $ZnSO_4$ without and with 0.5 wt% TAA additive. (d) and (e) The XRD patterns and (f) corresponding (100)/(002) peak ratios of Zn plating on the Cu substrate with various capacities (labelled in the center) in the two electrolytes. (g) GIWAXS patterns of Zn deposits in the two electrolytes. (h) The adsorption energies of the TAA molecule on the (002) and (100) planes of Zn. (i) The SEM images of Zn deposits in the two electrolytes.

The effect of TAA additive on the evolution of the morphology of Zn deposits on the Cu substrate is studied. Fig. 3d and e compare the XRD patterns at deposition capacities of 5, 10, and 15 mA h cm^{-2}. In the baseline $ZnSO_4$ electrolyte, the intensities of different diffractions grow anisotropically with an increase in deposition capacity. Upon the addition of 0.5 wt% TAA, a strongly preferred orientation is observed, as evidenced by the growth of the (100) peak and the negligible (002) peak. Using the (002) peaks as the benchmark, the intensity ratio of (100)/(002) peaks is as high as 22.6 at 5 mA h cm^{-2} deposition capacity, which further significantly increases to 174.4 at 15 mA h cm^{-2} (Fig. 3f). Conversely, the ratios remain low at around one in the baseline electrolyte. Grazing-incidence wide-angle X-ray scattering (GIWAXS) is used to further analyze the texture of the Zn deposits (Fig. 3g). At a deposition capacity of 15 mA h cm^{-2}, the pattern from the baseline $ZnSO_4$ electrolyte presents two rings corresponding to the (002) and (100) planes of Zn. In contrast, the pattern obtained from 0.5-TAA electrolyte presents a strong signal from the (100) plane, whereas the one from (002) is negligible. This strongly preferred orientation is attributed to the doubled adsorption energy of TAA on the (100) plane of Zn with respect to (002) (Fig. 3h). The TAA molecules thus have a large shielding effect on the (100) plane, whereas the Zn nucleation and growth on the (002) plane is preferred (Fig. S7†).[31] Fig. 3i shows the SEM images of Zn deposition morphology with a capacity of 15 mA h cm^{-2}. The deposits from the baseline $ZnSO_4$ are composed of irregular particles. In comparison, a compact morphology with a (100) preferred orientation is obtained upon the introduction of TAA, thanks to its effective regulation of deposition behaviors and inhibition of corrosion processes.

Benefiting from the above effects, the TAA additive enhances the cycling stability and reversibility of the Zn electrode. Continuous single plating/stripping is carried out at 2 mA cm^{-2} in symmetric Zn cells, with the 2 m $ZnSO_4$ baseline electrolyte or the addition of different percentages of TAA (Fig. 4a and S8†). In 2 m $ZnSO_4$, cell short-circuiting takes place when the capacity reaches 8.9 mA h cm^{-2}. In comparison, the capacity is extended to 24.4 mA h cm^{-2}, 40.8 mA h cm^{-2}, 34.1 mA h cm^{-2} and 20.3 mA h cm^{-2} following the addition of 0.2 wt%, 0.5 wt%,

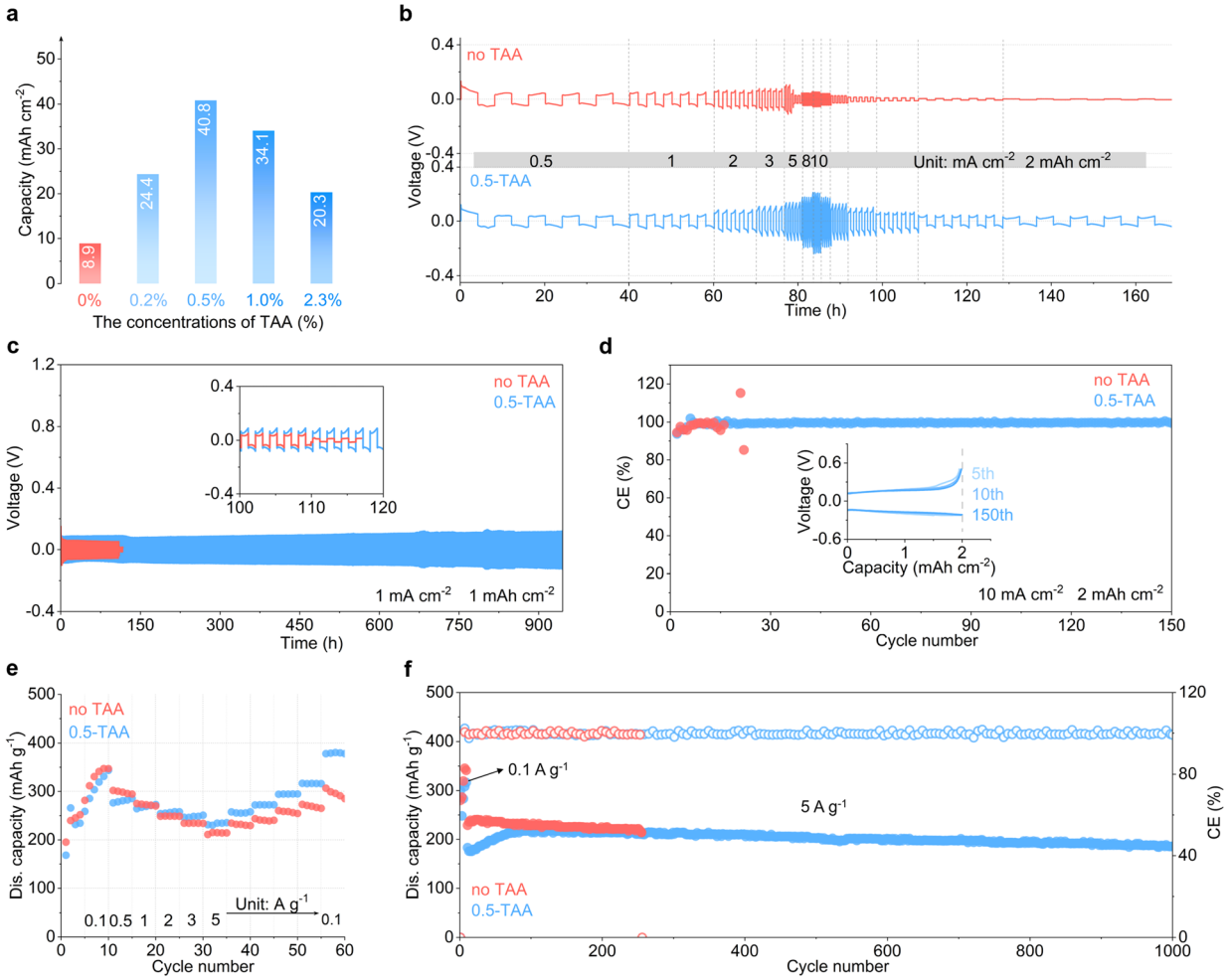

Fig. 4 Electrochemical performance of the Zn electrode in the 2 m $ZnSO_4$ electrolyte without and with 0.5 wt% TAA additive: (a) single deposition capacity with different TAA percentages; (b) rate performance and (c) long-term cycling stability of symmetric Zn cells; (d) coulombic efficiencies of Zn//Cu cells; (e) rate performance and (f) long-term cycling performance of Zn//V_2O_5 cells.

1.0 wt% and 2.3 wt% TAA, respectively. With the highest capacity obtained using 0.5 wt% additive, this concentration is identified as the optimal percentage. Repeated plating/stripping is further carried out in symmetric cells at different current densities with a capacity of 2 mA h cm^{-2}. As shown in Fig. 4b, cell short-circuit is observed when the current density increases to 5 mA cm^{-2} in the baseline electrolyte, as a result of the accumulation of inhomogeneous Zn deposits. In contrast, stable cycling takes place from 0.5 mA cm^{-2} to 10 mA cm^{-2} in the 0.5-TAA electrolyte. Long-term cycling is carried out at a current density of 1 mA cm^{-2} and capacity of 1 mA h cm^{-2} (Fig. 4c). In comparison to the cycle life of 110 h in the $ZnSO_4$ electrolyte, a 8.6 time extension to 945 h is obtained after the addition of 0.5 wt% TAA. The Zn plating/stripping coulombic efficiencies (CEs) are evaluated in Cu//Zn cells (Fig. 4d). The 0.5-TAA electrolyte delivers a stabilized CE of 99.55% for 150 cycles at 10 mA cm^{-2}, which is again superior to cell failure at the 16^{th} cycle in the TAA-free electrolyte.

To investigate the feasibility of the 0.5-TAA electrolyte for cathode materials, it is applied to a commercial V_2O_5 cathode in zinc cells. Fig. 4e compares the rate performance in the two electrolytes by galvanostatic charge–discharge. The V_2O_5 cathode experiences an activation process for ten cycles at 0.1 A g^{-1}. After activation in the baseline $ZnSO_4$ electrolyte, the cathode delivers 347 mA h g^{-1} capacity at 0.1 A g^{-1} but retains only 214 mA h g^{-1} with an increase in current density to 5 A g^{-1}. A poor capacity preservation of 285 mA h g^{-1} is obtained when the current density returns to 0.1 A g^{-1}. Closer examination of the capacity evolution suggests decay trends within each current density cycle, resulting in the decrease in capacity. With the addition of 0.5 wt% TAA, in contrast, the cathode realizes higher capacity as well as more stabilized retention within the same current density. As a result, it delivers a capacity of 343 mA h g^{-1} at 0.1 A g^{-1}, retains 235 mA h g^{-1} upon increasing the current density to 5 A g^{-1}, and achieves 378 mA h g^{-1} when the current density returns to 0.1 A g^{-1}. Long-term cycling is carried out at 5 A g^{-1} after 0.1 A g^{-1} activation. As shown in Fig. 4f, the TAA-free cell suffers soft short-circuit at the 255^{th} cycle. In 0.5-TAA, in contrast, stable cycling is achieved for 1000 cycles. This performance is comparable to that of previously reported Zn full cells (Table S1†).

The enhanced cycling stability of Zn//V_2O_5 cells upon the addition of TAA is studied further. Fig. S9† shows the SEM

images and EDS mappings of the cycled Zn anode. The one from the baseline $ZnSO_4$ electrolyte exhibits an uneven morphology with significant volume expansion, together with strong signals from S and O elements. This corresponds to inhomogeneous deposition and severe side reactions. In contrast, the anode from the 0.5-TAA electrolyte exhibits a uniform surface and weaker S/O signals. Conversely, the cycled cathodes from the two electrolytes show minimal differences (Fig. S10 and S11†). Fig. S12† shows the Nyquist plots at different cycles. The initial semi-circle in the baseline electrolyte is smaller than that in 0.5-TAA, attributed to the slower reaction kinetics and lower proton activity in the latter. The semi-circles decay upon cycling and remain stable after 200 cycles in the 0.5-TAA electrolyte. This is in good accordance with its stable cycling performance. The results suggest that the different stabilities of full cells are mainly caused by the anode. The uneven deposition and side reactions in the baseline electrolyte lead to instability of the Zn anode and early cell short-circuiting. Upon the introduction of TAA additive, in contrast, the improved anode stability enables extended cycle life. The results confirm that the TAA electrolyte additive effectively enhances the cycling stability of the Zn electrode as well as full cells.

Conclusions

In conclusion, we propose a 0.5 wt% TAA-based interface regulator with a claw structure for use in aqueous Zn batteries. The terminal amino groups on the TAA molecule allow strong interactions with the Zn surface and Zn^{2+} cations at the nearby interface. This provides uniform cation flux toward the Zn electrode. Meanwhile, the participation of TAA in the interfacial solvation shells of Zn^{2+} modifies the subsequent desolvation process. The release of solvated water is facilitated, and corrosion reactions are inhibited. The controlled desolvation of final TAA further modulates the deposition kinetics, allowing the generation of uniform Zn deposits. In addition, the stronger affinity of TAA on the Zn (100) plane promotes a preferred deposition orientation. Benefitting from these positive merits, the modified electrolyte significantly extends the cycle life of symmetric cells to 8.6 times compared to the baseline electrolyte, and simultaneously enhances the cycling stability of a Zn//V_2O_5 full battery. This work not only reveals an effective interface regulator for the Zn electrode, the uncovering its operating mechanisms would also contribute to the exploration of other electrolyte additives from fundamental molecular design to achieve highly reversible and stable aqueous Zn batteries.

Data availability

Data are available from the authors on reasonable request.

Author contributions

X. S. and K. W. conceived and designed this work. K. W., H. Z. and Q. L. carried out the electrochemical measurements and computational calculations. All authors participated in the analysis of the data, discussed and revised the manuscript.

Conflicts of interest

The authors declare no competing financial interests.

Acknowledgements

This work was supported by the National Natural Science Foundation of China (52174276, 51974070), the Central Guidance for Local Science and Technology Development Foundation (Youth Science Program Type A of Liaoning Province, 2025JH6/101100007), the Fundamental Research Funds for the Central Universities (N25QNR011, N232410019), and the 111 Project (B16009). Special thanks are due to the instrumental analysis from Analytical and Testing Center, Northeastern University.

References

1 K. Zhao, G. Fan, J. Liu, F. Liu, J. Li, X. Zhou, Y. Ni, M. Yu, Y.-M. Zhang, H. Su, Q. Liu and F. Cheng, Boosting the Kinetics and Stability of Zn Anodes in Aqueous Electrolytes with Supramolecular Cyclodextrin Additives, *J. Am. Chem. Soc.*, 2022, **144**, 11129–11137.

2 W. Sun, F. Wang, B. Zhang, M. Zhang, V. Küpers, X. Ji, C. Theile, P. Bieker, K. Xu, C. Wang and M. Winter, A rechargeable zinc-air battery based on zinc peroxide chemistry, *Science*, 2021, **371**, 46–51.

3 M. Shi, C. Lei, H. Wang, P. Jiang, C. Xu, W. Yang, X. He and X. Liang, Molecule Engineering of Sugar Derivatives as Electrolyte Additives for Deep-Reversible Zn Metal Anode, *Angew. Chem., Int. Ed.*, 2024, **63**, e202407261.

4 N. Wang, X. Dong, B. Wang, Z. Guo, Z. Wang, R. Wang, X. Qiu and Y. Wang, Zinc–Organic Battery with a Wide Operation-Temperature Window from −70 to 150 °C, *Angew. Chem., Int. Ed.*, 2020, **59**, 14577–14583.

5 K. Zhou, Z. Li, X. Qiu, Z. Yu and Y. Wang, Boosting Zn Anode Utilization by Trace Iodine Ions in Organic-Water Hybrid Electrolytes through Formation of Anion-rich Adsorbing Layers, *Angew. Chem., Int. Ed.*, 2023, **62**, e202309594.

6 X. Shen, W. Chen, H. Wang, L. Zhang, B. Hao, C. Zhu, X. Yang, M. Sun, J. Zhou, X. Liu, C. Yan and T. Qian, Selectively "size-excluding" water molecules to enable a highly reversible zinc metal anode, *Chem. Sci.*, 2024, **15**, 10182–10192.

7 M. Qiu, P. Sun, K. Han, Z. Pang, J. Du, J. Li, J. Chen, Z. L. Wang and W. Mai, Tailoring water structure with high-tetrahedral-entropy for antifreezing electrolytes and energy storage at −80 °C, *Nat. Commun.*, 2023, **14**, 601.

8 Z. Liu, J. Ma, X. Liu, H. Wu, D. Wu, B. Chen, P. Huang, Y. Huang, L. Wang, Z. Li and S. Chou, Coordinating zincophilic sites and a solvation shell for a dendrite-free Zn anode under the synergistic effects of polyacrylonitrile and dimethyl sulfoxide, *Chem. Sci.*, 2023, **14**, 2114–2122.

9 L. Wang, B. Zhang, W. Zhou, Z. Zhao, X. Liu, R. Zhao, Z. Sun, H. Li, X. Wang, T. Zhang, H. Jin, W. Li, A. Elzatahry, Y. Hassan, H. J. Fan, D. Zhao and D. Chao, Tandem Chemistry with Janus Mesopores Accelerator for Efficient Aqueous Batteries, *J. Am. Chem. Soc.*, 2024, **146**, 6199–6208.
10 Z. Liu, Z. Guo, L. Fan, C. Zhao, A. Chen, M. Wang, M. Li, X. Lu, J. Zhang, Y. Zhang and N. Zhang, Construct Robust Epitaxial Growth of (101) Textured Zinc Metal Anode for Long Life and High Capacity in Mild Aqueous Zinc-Ion Batteries, *Adv. Mater.*, 2024, **36**, 2305988.
11 H. Jiang, L. Tang, Y. Fu, S. Wang, S. K. Sandstrom, A. M. Scida, G. Li, D. Hoang, J. J. Hong, N.-C. Chiu, K. C. Stylianou, W. F. Stickle, D. Wang, J. Li, P. A. Greaney, C. Fang and X. Ji, Chloride electrolyte enabled practical zinc metal battery with a near-unity Coulombic efficiency, *Nat Sustainability*, 2023, **6**, 806–815.
12 W. Sun, V. Küpers, F. Wang, P. Bieker and M. Winter, A Non-Alkaline Electrolyte for Electrically Rechargeable Zinc-Air Batteries with Long-Term Operation Stability in Ambient Air, *Angew. Chem., Int. Ed.*, 2022, **61**, e202207353.
13 Y. Chai, X. Xie, Z. He, G. Guo, P. Wang, Z. Xing, B. Lu, S. Liang, Y. Tang and J. Zhou, A smelting–rolling strategy for ZnIn bulk phase alloy anodes, *Chem. Sci.*, 2022, **13**, 11656–11665.
14 Y. Dong, L. Miao, G. Ma, S. Di, Y. Wang, L. Wang, J. Xu and N. Zhang, Non-concentrated aqueous electrolytes with organic solvent additives for stable zinc batteries, *Chem. Sci.*, 2021, **12**, 5843–5852.
15 K. Fu, T. Liu, M. Xie, Y. Wu, Z. Li, Y. Xin, Y. Liao, C. Liu, H. Huang, D. Ma, F. Zeng and X. Liang, Water-Lean Inner Helmholtz Plane Enabled by Tetrahydropyran for Highly Reversible Zinc Metal Anode, *Adv. Funct. Mater.*, 2024, **34**, 2407895.
16 W. Sun, F. Wang, B. Zhang, M. Zhang, V. Küpers, X. Ji, C. Theile, P. Bieker, K. Xu, C. Wang and M. Winter, A rechargeable zinc-air battery based on zinc peroxide chemistry, *Science*, 2021, **371**, 46–51.
17 C. Huang, X. Zhao, Y. Hao, Y. Yang, Y. Qian, G. Chang, Y. Zhang, Q. Tang, A. Hu and X. Chen, Selection criteria for electrical double layer structure regulators enabling stable Zn metal anodes, *Energy Environ. Sci.*, 2023, **16**, 1721–1731.
18 R. Zhang, W. K. Pang, J. Vongsvivut, J. A. Yuwono, G. Li, Y. Lyu, Y. Fan, Y. Zhao, S. Zhang, J. Mao, Q. Cai, S. Liu and Z. Guo, Weakly solvating aqueous-based electrolyte facilitated by a soft co-solvent for extreme temperature operations of zinc-ion batteries, *Energy Environ. Sci.*, 2024, **17**, 4569–4581.
19 K. Wang, T. Qiu, L. Lin, H. Zhan, X.-X. Liu and X. Sun, A chelation process by an amino alcohol electrolyte additive to capture Zn2+ and realize parallel Zn deposition for aqueous Zn batteries, *Energy Storage Mater.*, 2024, **70**, 103516.
20 H. Qin, W. Kuang, N. Hu, X. Zhong, D. Huang, F. Shen, Z. Wei, Y. Huang, J. Xu and H. He, Building Metal-Molecule Interface towards Stable and Reversible Zn Metal Anodes for Aqueous Rechargeable Zinc Batteries, *Adv. Funct. Mater.*, 2022, **32**, 2206695.
21 K. Qiu, G. Ma, Y. Wang, M. Liu, M. Zhang, X. Li, X. Qu, W. Yuan, X. Nie and N. Zhang, Highly Compact Zinc Metal Anode and Wide-Temperature Aqueous Electrolyte Enabled by Acetamide Additives for Deep Cycling Zn Batteries, *Adv. Funct. Mater.*, 2024, **34**, 2313358.
22 L. Miao, R. Wang, S. Di, Z. Qian, L. Zhang, W. Xin, M. Liu, Z. Zhu, S. Chu, Y. Du and N. Zhang, Aqueous Electrolytes with Hydrophobic Organic Cosolvents for Stabilizing Zinc Metal Anodes, *ACS Nano*, 2022, **16**, 9667–9678.
23 C. Li, R. Kingsbury, A. S. Thind, A. Shyamsunder, T. T. Fister, R. F. Klie, K. A. Persson and L. F. Nazar, Enabling selective zinc-ion intercalation by a eutectic electrolyte for practical anodeless zinc batteries, *Nat. Commun.*, 2023, **14**, 3067.
24 H. Li, L. Yang, S. Zhou, J. Li, Y. Chen, X. Meng, D. Xu, C. Han, H. Duan and A. Pan, A Self-Regulated Interface Enabled by Multi-Functional pH Buffer for Reversible Zn Electrochemistry, *Adv. Funct. Mater.*, 2024, **34**, 2313859.
25 H. Li, Y. Ren, Y. Zhu, J. Tian, X. Sun, C. Sheng, P. He, S. Guo and H. Zhou, A Bio-Inspired Trehalose Additive for Reversible Zinc Anodes with Improved Stability and Kinetics, *Angew. Chem., Int. Ed.*, 2023, **62**, e202310143.
26 T. Wu, C. Hu, Q. Zhang, Z. Yang, G. Jin, Y. Li, Y. Tang, H. Li and H. Wang, Helmholtz Plane Reconfiguration Enables Robust Zinc Metal Anode in Aqueous Zinc-Ion Batteries, *Adv. Funct. Mater.*, 2024, **34**, 2315716.
27 Y. Liang, M. Qiu, P. Sun and W. Mai, Janus interface enables reversible Zn-ion battery by regulating interfacial water structure and crystal-orientation, *Chem. Sci.*, 2024, **15**, 1488–1497.
28 M. Luo, C. Wang, H. Lu, Y. Lu, B. B. Xu, W. Sun, H. Pan, M. Yan and Y. Jiang, Dendrite-free zinc anode enabled by zinc-chelating chemistry, *Energy Storage Mater.*, 2021, **41**, 515–521.
29 K. Wang, H. Zhan, W. Su, X.-X. Liu and X. Sun, Ordered interface regulation at Zn electrodes induced by trace gum additives for high-performance aqueous batteries, *Energy Environ. Sci.*, 2025, **18**, 1398–1407.
30 Y. Ma, Q. Ma, Y. Liu, Y. Tan, Y. Zhang, N. Han, S. Bao, J. Song and M. Xu, Multiphilic-Zn group "adhesion" strategy toward highly stable and reversible zinc anodes, *Energy Storage Mater.*, 2023, **63**, 103032.
31 T. Wei, Y. Ren, Y. Wang, L. e. Mo, Z. Li, H. Zhang, L. Hu and G. Cao, Addition of Dioxane in Electrolyte Promotes (002)-Textured Zinc Growth and Suppressed Side Reactions in Zinc-Ion Batteries, *ACS Nano*, 2023, **17**, 3765–3775.